Available online at www.sciencedirect.com
ScienceDirect
Journal of Sound and Vibration 324 (2009) 751–772
JOURNAL OF SOUND AND VIBRATION
www.elsevier.com/locate/jsvi

Guided wave propagation and spectral element method for debonding damage assessment in RC structures

Ying Wang[a,b], Xinqun Zhu[c,*], Hong Hao[a], Jinping Ou[b]

[a]*School of Civil and Resource Engineering, CRC for Integrated Engineering Asset Management, The University of Western Australia, Crawley, WA 6009 Australia*
[b]*School of Civil Engineering, Harbin Institute of Technology, Harbin 150090, China*
[c]*School of Engineering, The University of Western Sydney, Penrith South DC, NSW1797, Australia*

Received 27 March 2008; received in revised form 3 September 2008; accepted 22 February 2009
Handling Editor: L.G. Tham
Available online 24 March 2009

Abstract

A concrete–steel interface spectral element is developed to study the guided wave propagation along the steel rebar in the concrete. Scalar damage parameters characterizing changes in the interface (debonding damage) are incorporated into the formulation of the spectral finite element that is used for damage detection of reinforced concrete structures. Experimental tests are carried out on a reinforced concrete beam with embedded piezoelectric elements to verify the performance of the proposed model and algorithm. Parametric studies are performed to evaluate the effect of different damage scenarios on wave propagation in the reinforced concrete structures. Numerical simulations and experimental results show that the method is effective to model wave propagation along the steel rebar in concrete and promising to detect damage in the concrete–steel interface.

1. Introduction

Reinforced concrete (RC) structures are widely used in civil infrastructure systems due to its low construction cost and long service life under various conditions. The interface between concrete and steel in RC governs the interaction between the two types of materials under loading. When the interface is seriously damaged, e.g. when a micro-crack is formed, debonding takes place with large slip, and the load-transferring capacity of the interface will drop dramatically. Soh et al. [17] presented a damage model, which included the normal and tangential damage factors, to describe the concrete–steel interface mechanism. A RC element is developed based on this damage model to simulate the bond deterioration in RC structures [18]. Zhu and Law [21] developed a concrete–steel interface element for damage detection of RC structures from static responses. However, the bonding loss is insensitive to the static or low-frequency structural responses and it is significantly more difficult to be detected than damages occurring on concrete such as cracks and loss of cross

*Corresponding author. Tel.: +61 08 64887051.
E-mail addresses: zhu@civil.uwa.edu.au, xinqun.zhu@uws.edu.au (X. Zhu).

0022-460X/$ - see front matter © 2009 Elsevier Ltd. All rights reserved.
doi:10.1016/j.jsv.2009.02.028

sections. On the other hand, the guided wave (GW) based methods generate a fairly high frequency pulse to the structure, which make minor damage detection become possible.

GW can be defined as stress waves forced to follow a path defined by the material boundaries of a structure. Due to its capacity of relatively long propagation range as well as its flexibility in selecting sensitive mode-frequency combinations, GW has been found as an effective and efficient way to detect incipient damages in civil, mechanical and aerospace structures recently. Raghavan and Cesnik [16] presented a literature review for GW based structural health monitoring. The majority of research has focused on damage sources such as delamination, low velocity impact and debond in sandwich and stiffened CFRP structures [5]. The piezoelectric materials are widely used for exciting and measuring GWs in structural health monitoring. With the use of built-in actuators and sensors, the GW based approach is complementary to development of integrated systems for continuous on-line monitoring [7]. Recently, it is used to detect the delamination at the interface between steel bars and concrete [12,19]. Further theoretical analysis is needed to quantify the delamination at the interface between the concrete and steel bars.

Wave propagation analysis has been extensively used for structural health monitoring. Proper use of these techniques requires good knowledge of the effects of damage on the wave characteristics. This needs accurate and computationally efficient modeling of the damaged structures. A number of different numerical computational techniques can be used for the analysis of wave propagation. In contrast to wave propagation studies, wave interaction with damage has found less attention. The global matrix approach [8] is used to model an elastic hollow cylinder coated with a viscoelastic material [1]. It is further applied to quantifying the reflection and transmission coefficients of discontinuities in waveguides from measured data [11]. In this approach, there is no explicit relationship between the reflection or transmission coefficients and the damage extent. Finite element method is normally used to model wave propagation in the time domain [10,20]. It may provide accurate dynamic characteristics of a structure if the wavelength is large as compared to the mesh size. However, the finite element solutions become increasingly inaccurate and inefficient as the frequency increases. This is because the wavelengths are very small at high frequencies, which requires a very fine finite element mesh size for a reliable modeling. Hence, finite element formulation for wave propagation problems requires large system size to capture the high frequency waves.

The problem can be solved in the frequency domain. One such method is the spectral element method (SEM) [2]. In SEM, the governing partial differential equations (PDEs) are transferred to ordinary differential equations (ODEs) in spatial dimension by using FFT. These ODEs are then solved exactly, which are used as interpolation functions for the spectral element formulation. The use of exact solution in the element formulation ensures the exact mass and stiffness distribution. It means that only one element needs be used for modeling a very large part of a structure, under the condition that this part has no discontinuities. Hence, the required number of elements is much less in comparison to the conventional finite element formulation. Palacz and Krawczuk [14] presented a rod spectral finite element with a transverse open and non-propagation crack. The influence of the crack growth on the wave propagation is examined using SEM. Palacz et al. [15] examined the effect of an additional mass placed on an isotropic rod using the changes in wave propagation, and developed a spectral element for isotropic rod with an additional mass. Ostachowicz [13] gives an informative review of the principles, equations and applications of damage modeling and elastic wave propagation in a cracked rod, a beam and a plate. Mitra and Gopalarishnan [9] used the Daubechies scaling functions for approximation in the time domain for reduction of PDEs to ODEs, and developed a wavelet-based spectral finite element method for modeling and detection of de-lamination in composite beams.

In this study, a concrete–steel interface spectral element is developed to model the GW propagation along a steel rebar in the concrete. Scalar damage parameters characterizing changes of the interface conditions are incorporated into the formulation of the spectral finite element. It is then used to detect and assess debonding damages along the rebar and concrete interface. Experimental tests are carried out on a RC beam with embedded piezoelectric elements. The piezoelectric elements are used to generate a high frequency pulse force on the rebar and to record the GW propagation along the rebar. Test results are compared with the numerical simulation results to check the performance of the proposed model and algorithm. Parametric simulations are also performed to evaluate the effect of different damage scenarios on the wave propagation in the RC structures. Numerical simulations and experimental results show that the method is effective to model wave propagation along the steel rebar in concrete and can be used to detect damage in the concrete–steel interface.

2. Spectral finite element for RC structures

2.1. Concrete–steel interface spectral element

In this study, the piezoelectric elements are mounted on steel bars embedded in concrete and these elements are used to generate and receive the wave signal. In order to explore the wave propagation along the rebar in the concrete, a novel spectral element is needed to describe the wave propagation at the interface between the steel bars and concrete. For RC structures, the length of the steel rebar is much larger than its radius, so it is modeled as an ideal rod in this study. Though there are several rod theories with different number of modes, elementary theory is accurate enough to simulate the wave propagation on the condition that the frequency of the transmitting wave is lower than 100 kHz [6], which is within the scope of this study.

In this section, it is assumed that concrete will deform axially under the shear force from steel rebar. The cross section of the beam and their force analysis are illustrated in Fig. 1. Based on elementary theory [2,3], the equations of steel and concrete motion can be written as follows:

$$E_s A_s \frac{\partial^2 u_s(x,t)}{\partial x^2} = \rho_s A_s \frac{\partial^2 u_s(x,t)}{\partial t^2} + \eta_s A_s \frac{\partial u_s(x,t)}{\partial t} + q(x) \tag{1}$$

$$q(x) = E_c A_c \frac{\partial^2 u_c(x,t)}{\partial x^2} + \rho_c A_c \frac{\partial^2 u_c(x,t)}{\partial t^2} + \eta_c A_c \frac{\partial u_c(x,t)}{\partial t} \tag{2}$$

where $u_s(x,t)$, $u_c(x,t)$ are the axial displacements of the steel rebar and concrete at location x and time t. E_s, E_c denote the Young's modulus of the steel and concrete. A_s and A_c are the areas of the cross sections corresponding to the steel and concrete; respectively. Here A_c should be defined as the effective area of concrete, which will be explained later. ρ_s, ρ_c are the densities of the steel and concrete. η_s, η_c are the viscous damping ratios of the steel and concrete, which are used to simulate the material damping. Usually, a small value of η is used as follows [2]:

$$\eta_s = \rho_s \omega_0 \times 10^{-3}, \quad \eta_c = \rho_c \omega_0 \times 10^{-3} \tag{3}$$

where ω_0 is a circular frequency. The typical frequency used in this study is 30–60 kHz.

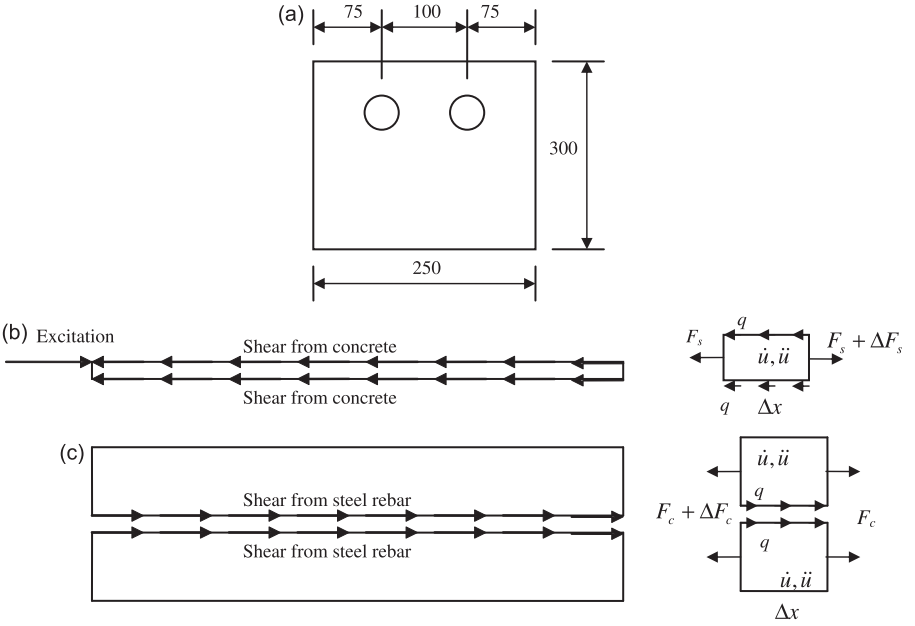

Fig. 1. Concrete–steel interface spectral element: (a) cross section of concrete beam; (b) force on steel rebar; (c) force on concrete based on axial deformation assumption.

Combining Eqs. (1) and (2) together, one can obtain

$$(E_sA_s - E_cA_c)\frac{\partial^2 u}{\partial x^2} = (\rho_sA_s + \rho_cA_c)\frac{\partial^2 u}{\partial t^2} + (\eta_sA_s + \eta_cA_c)\frac{\partial u}{\partial t} \tag{4}$$

To further simplify the above equation, the following equivalent parameters are defined

$$E = E_{eq} = \frac{E_sA_s - E_cA_c}{A}$$

$$\rho = \rho_{eq} = \frac{\rho_sA_s + \rho_cA_c}{A}$$

$$\eta = \eta_{eq} = \frac{\eta_sA_s + \eta_cA_c}{A} \tag{5}$$

where $A = A_{eq} = A_s + A_c$.

Using the equivalent parameters defined in Eq. (5), Eq. (4) can be written as follows:

$$EA\frac{\partial^2 u(x,t)}{\partial x^2} = \rho A\frac{\partial^2 u(x,t)}{\partial t^2} + \eta A\frac{\partial u(x,t)}{\partial t} \tag{6}$$

In order to solve Eq. (6), the dynamic responses are expressed in the spectral representation [2] as:

$$u(x,t) = \sum_n^N \hat{u}(x,\omega_n)\mathrm{e}^{\mathrm{j}\omega_n t} \tag{7}$$

where $\mathrm{j} = \sqrt{-1}$ and $\hat{u}(x,\omega_n)$ is the spatially dependent Fourier coefficient.

For every ω_n, Eq. (6) can be written as:

$$EA\frac{\partial^2 \hat{u}}{\partial x^2} + (\omega_n^2\rho A - \mathrm{j}\omega_n\eta A)\hat{u} = 0 \tag{8}$$

where $\hat{u}$ is the abbreviation of $\hat{u}(x,\omega_n)$.

From Eq. (8), the general longitudinal displacement (with the exponential solution $\mathrm{e}^{-\mathrm{j}kx}$) for a rod can be written as:

$$\hat{u}(x) = B\mathrm{e}^{-\mathrm{j}kx} + C\mathrm{e}^{+\mathrm{j}kx}, \quad k = \pm\sqrt{\frac{\omega^2\rho A - \mathrm{j}\omega\eta A}{EA}} \tag{9}$$

where B, C denote the amplitudes of inward and outward waves, respectively, which will be determined by boundary conditions, and k is the wavenumber.

Through the bond, concrete and steel can work together. But in reality, concrete will not deform uniformly over the cross section. Only the concrete near the steel bar will have similar deformation as the steel rebar, and the deformation decreases along the cross section away from the steel bar towards the concrete surface. Therefore, the axial deformation of the concrete beam is not uniform over the cross section. Based on the axial deformation assumption and stress equilibrium, an equivalent area A_c is then defined, which can be obtained from the wave speed. Since η is very small, the wave speed along the steel rebar in concrete can be represented as follows:

$$c = \sqrt{\frac{EA}{\rho A}} = \sqrt{\frac{E_sA_s - E_cA_c}{\rho_sA_s + \rho_cA_c}} \tag{10}$$

Thus,

$$A_c = \frac{E_s - \rho_s c^2}{E_c + \rho_c c^2} A_s \tag{11}$$

In practice, c can be measured easily. Based on Eq. (11), A_c can be obtained, and the proper parameters, E, A, η and ρ, can be calculated by Eq. (5). Since A_c changes with the radius of steel bar, the quality of concrete, the interface condition and others, it is very complicated to formulate an empirical function for it. The best determination method is to extract the wave speed from the measured signal of the intact structure.

2.2. Generalized SEM

The above equations describe wave propagation in a concrete–steel interface spectral element with homogeneous properties. When the interface has non-uniform properties such as changing material or sectional properties along its length owing to damages associated with material deterioration, corrosion and/or cracks, the reflection and transmission coefficients will be different in different segments. The damaged zones need be formulated accordingly with their respective properties, hence multiple spectral elements are necessary. A generalized model for multiple spectral elements is displayed in Fig. 2. The spectral displacement of the ith element can be defined as follows:

$$\hat{u}_i(x) = B_i e^{-jk_i x} + C_i e^{-jk_i(\sum_{p=1}^{i} L_p - x)} \quad \text{for } x \in \left(L - \sum_{p=i}^{N} L_p, \sum_{p=1}^{i} L_p \right) \tag{12}$$

where L represents the length of the rebar, L_p is the length of the pth element.

If the actuator and sensor are located in the middle of the rebar at locations a and b, respectively, the structure should at least be discretized into 3 elements with the actuator and sensor in the first and the last element, and the locations of the two elements being $x_a = L_1$ and $x_b = L - L_N$. Generally, for N elements, there are $2N$ unknown coefficients $\{B_i, C_i, i = 1, 2, \ldots, N\}$, which can be calculated as a function of the nodal spectral displacements. The following boundary conditions are taken into account.

(a) At the left end of the 2nd element ($x_a = L_1$)

$$\hat{u}_2(x_a) = \hat{q}_a \tag{13}$$

where $\hat{q}_a$ is the nodal displacement at location a (actuator).

(b) At the right end of an intermediate element i, the displacement and strain compatibility leads to

$$\hat{u}_{i+1}\left(L - \sum_{p=i+1}^{N} L_p \right) - \hat{u}_i \left(\sum_{p=1}^{i} L_p \right) = 0$$

$$\frac{\partial \hat{u}_{i+1}\left(L - \sum_{p=i+1}^{N} L_p \right)}{\partial x} - \frac{\partial \hat{u}_i \left(\sum_{p=1}^{i} L_p \right)}{\partial x} = 0 \tag{14}$$

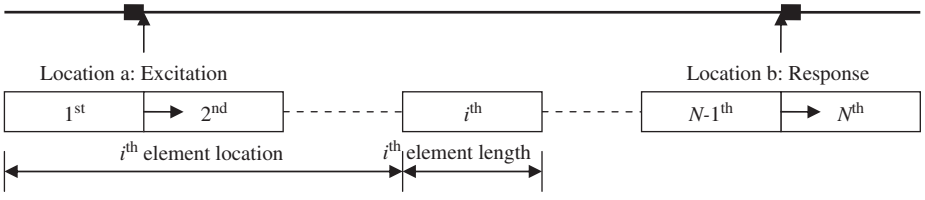

Fig. 2. The generalized model of the rod with arbitrary elements.

(c) At the right end of the 2nd last element ($x_b = L - L_N$)

$$\hat{u}_{N-1}(x_b) = \hat{q}_b \tag{15}$$

where $\hat{q}_b$ is the nodal displacement at location b (sensor).

The above formulae can be rewritten in the matrix form as follows

$$D \cdot G = Q \tag{16}$$

where D is the boundary matrix, which can be derived from Eqs. (13)–(15), N is the number of the elements, $G = \{B_1, C_1, \ldots, B_i, C_i, \ldots, B_N, C_N\}^{\mathrm{T}}$, $Q = \{\hat{q}_a, \ldots, \hat{q}_b\}^{\mathrm{T}}$. By updating L_i according to the measured wave signal, the damage lengths and locations can be determined. As an example, a 5-elements model is adopted for a structure with one damage zone. The boundary matrix D of 5 elements is given in Appendix A.

Then, parameters B_i, C_i can be obtained using the inverse matrix of D.

$$G = D^{-1} \cdot Q \tag{17}$$

Based on Eq. (12), the force boundary conditions can be represented as:

$$\begin{bmatrix} \hat{F}_a \\ \hat{F}_b \end{bmatrix} = \begin{bmatrix} \hat{F}_2 \\ \hat{F}_{N-1} \end{bmatrix} = EA \cdot \begin{bmatrix} 0 & 0 & -\mathrm{i}k_2 \mathrm{e}^{-\mathrm{i}k_2 L_1} & \mathrm{i}k_2 \mathrm{e}^{-\mathrm{i}k_2 L_2} & 0 & \cdots & 0 & 0 & 0 & 0 \\ 0 & 0 & 0 & 0 & 0 & \cdots & -\mathrm{i}k_{N-1} \mathrm{e}^{-\mathrm{i}k_{N-1}(L-L_N)} & \mathrm{i}k_{N-1} & 0 & 0 \end{bmatrix} \cdot G \tag{18}$$

where $\hat{F}_a, \hat{F}_b$ are the nodal forces at locations a and b.

From Eqs. (17) and (18), the force–displacement can be simplified as follows:

$$\begin{bmatrix} \hat{F}_a \\ \hat{F}_b \end{bmatrix} = \begin{bmatrix} s_{aa} & s_{ab} \\ s_{ba} & s_{bb} \end{bmatrix} \cdot \begin{bmatrix} \hat{q}_a \\ \hat{q}_b \end{bmatrix} \tag{19}$$

Due to the inherent requirement of FFT, a throw-off element needs be added to the last element, which act as a conduit to allow the propagation of the trapped energy out of the system. As a result, Eq. (19) becomes:

$$\begin{bmatrix} \hat{F}_a \\ \hat{F}_b \end{bmatrix} = \begin{bmatrix} s_{aa} & s_{ab} \\ s_{ba} & s_{bb} + ik_N EA \end{bmatrix} \cdot \begin{bmatrix} \hat{q}_a \\ \hat{q}_b \end{bmatrix} = S \cdot \begin{bmatrix} \hat{q}_a \\ \hat{q}_b \end{bmatrix} \tag{20}$$

When $\hat{F}_a$ and $\hat{F}_b$ are known, $\hat{q}_a, \hat{q}_b$ can be easily obtained by Eq. (20). Based on this method, wave propagation can be easily modeled regardless of the number of elements.

2.3. Damage indices

For a structure with homogeneous material, damage in the structure is often defined as the loss of elastic modulus. But two materials with different properties work together in RC structures. Therefore, the performance of RC relies on not only the steel rebar and concrete but also their interaction. If they bond well, the force can be easily transferred from concrete to steel, and vice versa. But if debonding occurs, force transfer is not as easy as before, and slip may occur, which will impede the composite action of RC and bring down the performance of the structure severely.

In the proposed SEM, A_c is the variable which can provide some indications of debonding damage. In this study, the debonding damage index and conventional damage indices are defined as follows:

$$\alpha_b = 1 - \frac{A_c'}{A_c}$$

$$\alpha_s = 1 - \frac{E_s'}{E_s}$$

$$\alpha_c = 1 - \frac{E'_c}{E_c} \tag{21}$$

where A'_c is the unknown real effective area of concrete. E'_c, E'_s are the damaged elastic moduli for concrete and steel, respectively. When there is no debonding nor damage to concrete and steel rebar, $A'_c = A_c$, $E'_c = E_c$, $E'_s = E_s$ and $\alpha_b = \alpha_c = \alpha_s = 0$. When full debonding occurs, $A'_c = 0$, or full damage to concrete or steel rebar, $E'_c = 0$, $E'_s = 0$, then $\alpha_b = \alpha_c = \alpha_s = 1$. In other cases, $0 < \alpha_b, \alpha_c, \alpha_s < 1$.

3. Laboratory study

In order to verify the proposed model, an active sensing system using embedded piezoelectric components is built in laboratory and the experimental study is carried out on bare steel bars and RC beams.

3.1. Experimental setup

The experimental system, shown in Fig. 3, includes two parts: (a) the actuating part is to provide the excitation or input of the system. It includes the actuator based on piezoelectric strips and the power amplifier that provides the power supply of the actuator; (b) the piezo sensing element is to measure the response. This part includes the piezo film element and its charge amplifier.

The actuators were mounted on the surface of the steel reinforcing bar with Araldite Kit K138 and the steel bars were cast into a concrete beam to evaluate the delamination between the steel bars and concrete. The strip actuators from APC International, Ltd. were selected as actuators in this study. The actuator includes two thin strips of piezoelectric ceramic that are bonded together, with the direction of polarization coinciding with each other and are electrically connected in parallel. When electrical input is applied, one ceramic layer expands and the other contracts, causing the actuator to flex. In this study, only one ceramic layer was applied with the electrical input so that it would generate the wave. NI USB-6251 was used to provide the short-time Morlet wavelet for actuating the structure by a linear power amplifier. The frequency and the number of cycles can be adjusted to optimize the wave propagation along the steel bars. The waves were generated as above by the following equation:

$$\psi(t) = A\mathrm{e}^{-t^2/2\sigma^2}\cos(2\pi f t + \varphi) \tag{22}$$

where f is the centre wavelet frequency, σ is the bandwidth parameter and controls the shape of the basic wavelet. φ is the phase. Normally, the waveform is defined in $\pm 3\sigma$, and the number of cycles n is $n = 6\sigma f$. 6σ is the time duration of the waveform. Because wave signals decay quickly in concrete structures, the signal input

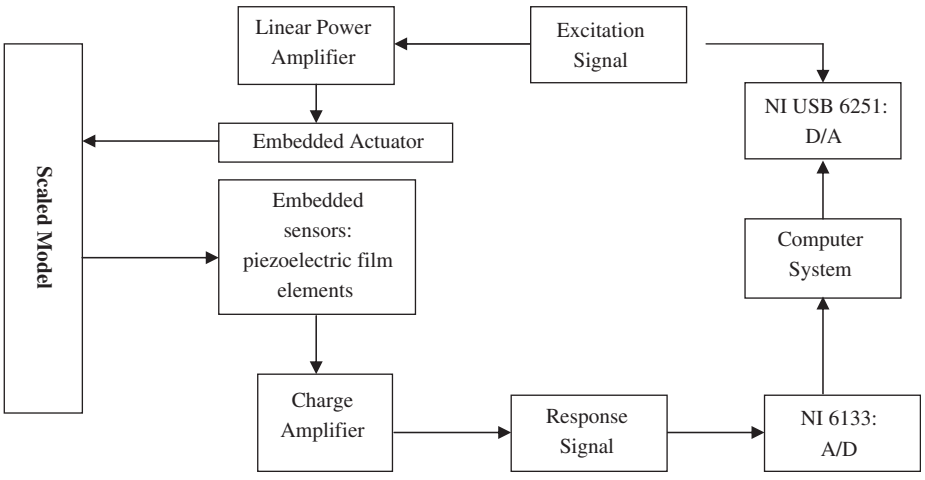

Fig. 3. Experimental system scheme.

on the actuators should be as strong as possible to generate readable output at the sensors. A linear power amplifier was developed to amplify the signals from the output of NI USB 6251.

The DT1 series piezo film elements from Measurement Specialties, Inc. were selected as the sensors. The sensors were also glued to the steel bars with Araldite Kit K138. Signals from sensors were collected by a data acquisition system made with NI PCI-6133. The sampling frequency of the system is up to 2 MHz. A program based on Labview was developed to control NI USB-6251 and make the two NI PCI-6133 cards work simultaneously.

3.2. Experimental results

In order to understand the wave propagation along the steel bar with or without concrete coating, six 1.5 m long RC beams were fabricated in laboratory. The cross section of these concrete beams is 0.25 m wide and 0.30 m high, as shown in Fig. 1(a). There are two steel plain round bars in each concrete beam. The material parameters of the steel bars are: Young's modulus 210 GPa, and mass density 7850 kg/m^3. The whole length of the steel rebar is 1.6 m with 1.5 m buried in the concrete and 0.05 m free end outside of the concrete beam on each side. The reason to leave 0.05 m long rebar outside is for the convenience of the subsequent corrosion tests, which is not within the scope of this study. The diameter of the steel bar is 0.01 m. The actuator and sensor were mounted on each steel round bar with 0.3 m from the two ends of the bar, respectively. The distance between the actuator and the sensor is 1 m. The wave propagation tests were carried out on the bare steel bars first. Then these steel bars were cast into the concrete beams. The location of steel rebar is shown in Fig. 1(a). The thickness of the concrete cover over steel bars is 0.05 m. The properties of concrete from material tests are: the compressive strength—39.70 MPa, the Young's modulus—29.61 GPa, and mass density—2426.75 kg/m^3. By the pull-out tests, the debonding strength is 0.21 MPa for the plain round steel bar. The wave propagation tests were carried out on these concrete beams after 28 days. The frequency of the transmitted waves is 50 kHz and the number of the wave cycles is 5. The sampling frequency for data recording is 2 MHz.

In this study, only the measured data on three steel bars is analysed and discussed in detail. Results from other steel bars are similar, but are not shown here. Fig. 4 shows the wave propagation along the three bare

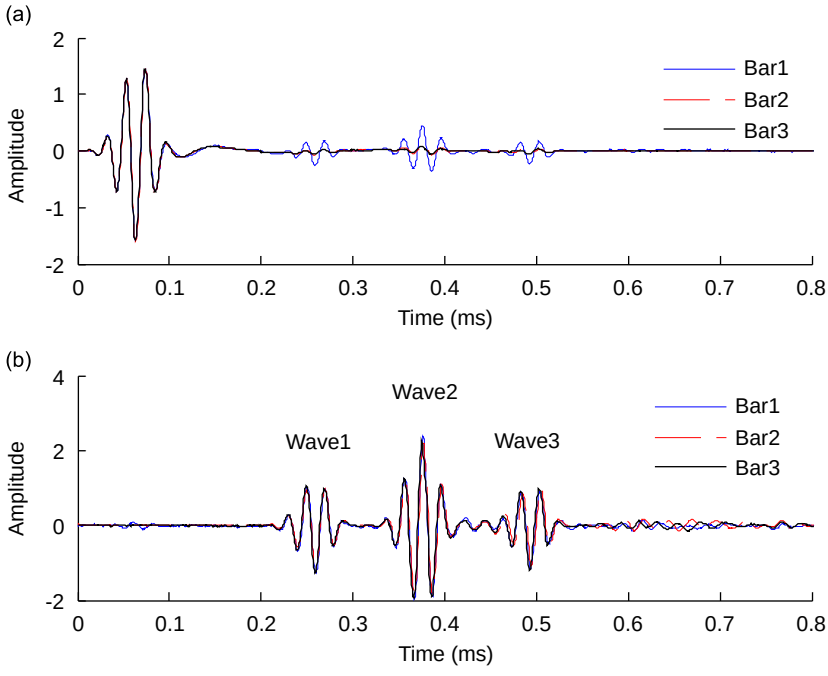

Fig. 4. Wave propagation along the bare steel bar: (a) excitation; (b) response.

steel bars. In the figure, the responses from the three bare steel bars are close to each other when the input signal is the same. This shows the system is reliable and stable to carry out the experimental study for wave propagation. There are mainly three waves in the response. Compared with the input signal, the time interval between the excitation source and the arrival of the waves are 0.20, 0.31 and 0.43 ms, respectively. The peak values of the three waves are 1.262, 2.371 and 1.109 V. Wave1 is the incident wave from the input, and Wave2 and Wave3 are the reflected waves by the two ends of the steel bar. Since the distance between the actuator and the left end is the same as that between the sensor and the right end, Wave2 is a combination of the two reflected waves from the two ends. The wave propagation distances of these three waves from the actuator are 1.0, 1.6 and 2.2 m, respectively. So the wave speeds from these waves are 5102.0, 5111.8, 5140.2 m/s, respectively. In Fig. 4(b), there are some small waves after the three main waves. They are the dispersive waves due to non-uniformality or defects in the steel bar itself. These dispersive waves are also useful to detect damages in the steel bar.

Fig. 5(a) shows the wave propagation along the steel bar in concrete beams. The first waves are again close to each other, and the following waves are much complicated because of the complex interaction and many reflections at the end of the concrete beam. Fig. 5(b) shows the comparison between the result from the bare steel bar and that buried in the concrete. Compared with the wave propagation along the bare steel bar,

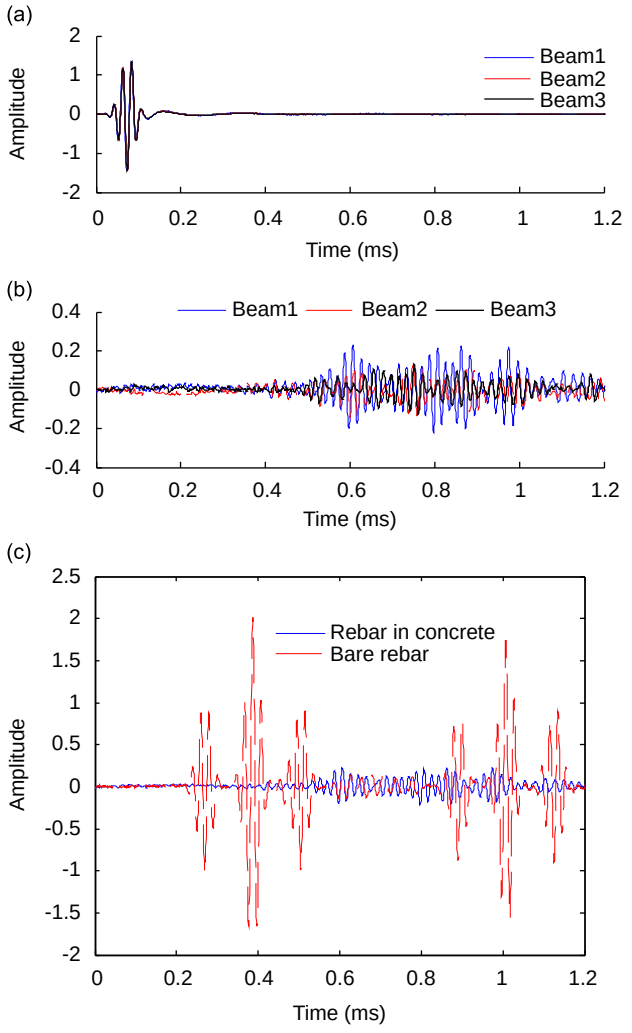

Fig. 5. Wave propagation in different waveguide: (a) excitation; (b) response; (c) comparison of wave propagation along the rebar in concrete or bare rebar.

the first wave is delayed when the steel bar is buried in the concrete and the amplitude is also much smaller, clearly indicating the interaction effect of steel and concrete.

3.3. Model verification

Steel bar can be easily modeled using a uniform material model, while concrete material is more complex, since it is a composite material that consists of sand, cement, and various sizes of aggregates. To simplify the analysis, however, a linear, elastic, isotropic and homogeneous model is adopted in numerical simulation. The damping ratios of steel and concrete are estimated from Eq. (3), their effect on the waveform will be discussed in the following section. Based on Fig. 5(a), the time interval between the excitation source and the arrival of the first wave is 0.445 ms. Since the distance between the actuator and the sensor is 1 m, the wave speed can be obtained as 2247 m/s. Based on Eq. (11), $A_c = 3.394 \times 10^{-4}\,\mathrm{m}^2$. As a result, the equivalent radius of the effective concrete is 0.0204 m, which is smaller than the cover thickness and distance between bars. Then, the parameters for concrete–steel interface spectral element can be obtained through Eq. (5), with $E = 15.42\,\mathrm{GPa}$, $\rho = 3446.10\,\mathrm{kg/m}^3$, and $\eta = 1.083 \times 10^6$.

In order to verify the numerical model in this study, the above tests are numerically simulated using the above parameters. Fig. 6 shows the comparison between the experimental results and the numerical results. Since the actuator and sensor are located in the middle of steel rebar, the 5-element model is used to analyse the wave propagation in a bare steel rebar. As shown, the calculated wave is very close to the first wave of the experimental result, demonstrating that the proposed model is effective to analyse the wave propagation in the bare steel bar. In the numerical simulation, the throw-off element is used to let the wave energy propagate out of the system, so there is no reflected wave. Simulation without considering damping effect is also carried out. The result is shown in Fig. 6 for comparison. As shown, the amplitude of the calculated wave without the damping is larger than that with the damping, but there is no obvious change in the waveform. The result shows that the damping has a large effect on the wave amplitude but little effect on the waveform.

The proposed 5-element model is applied to the steel rebar in concrete beam. Fig. 7 shows the experimental and numerical results for a steel bar in a concrete beam. From Fig. 7, the calculated incident wave is also close to the measured incident wave. It shows that the proposed model and algorithm is effective and accurate to analyse the wave propagation in concrete–steel interface.

4. Parametric study

In order to study the feasibility of GW-based damage identification of debonding damage in RC structures, the effect of different debonding damage on the received wave is studied using the proposed numerical model.

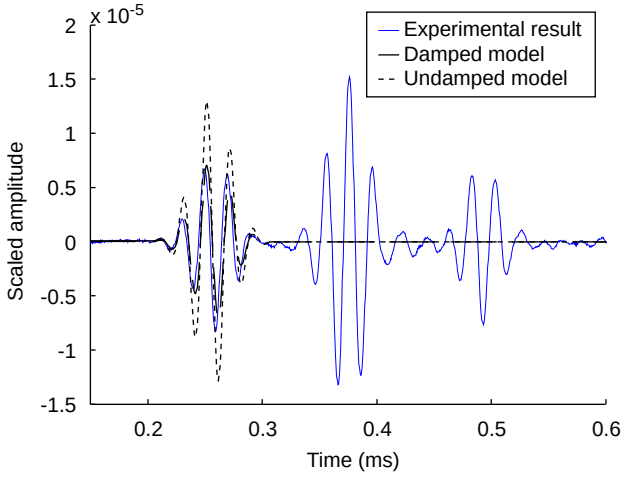

Fig. 6. Wave propagation in a bare steel bar.

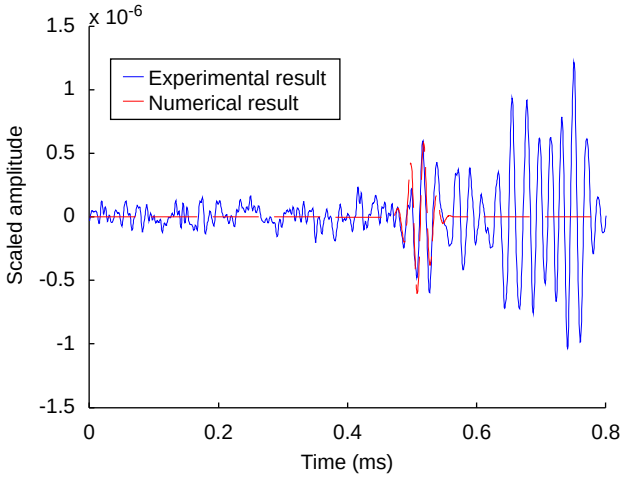

Fig. 7. Wave propagation along steel rebar in concrete beam.

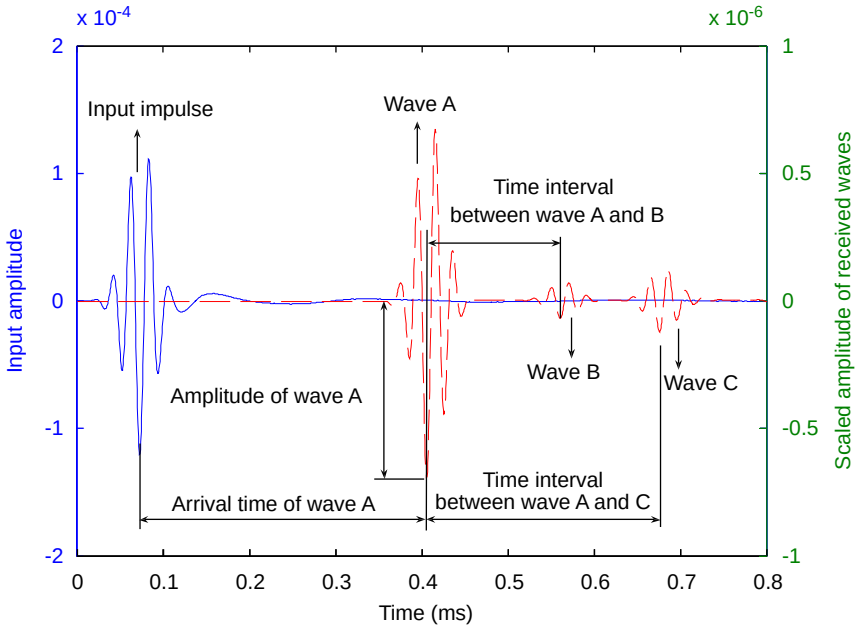

Fig. 8. Illustration of received waves and the corresponding parameters.

The above parameters of the test model are used in the calculation. Three parameters, namely debonding length, location and level, are used to describe the debonding damage. The debonding level is defined as a debonding damage index in Eq. (21) by the real effective area of concrete around the steel bar. The debonding damage zone is defined as a damaged element, as shown in Fig. 2. The debonding length and location correspond to the length and location of the damage element. Different debonding damage scenarios are simulated by changing the debonding length, location and level. The effect of damage in concrete or steel bar on waveform is also investigated by changing the damage indices α_c, α_s in the element.

In this section, the changes in the incident wave due to damage in the RC structure are investigated. The change in the incident wave and the feature parameters that will be extracted from the incident wave and are sensitive to the debonding damage need be defined first. Giurgiutiu and Cuc [4] performed the damage detection analysis in a structure through examining the changes of the GW amplitude, phase, dispersion and time of flight using the pitch-catch method. Guided wave propagation along the steel bar buried in concrete is

much complicated. Fig. 8 shows a typical wave propagation process from the input signal to the response. There are three waves, namely Waves A, B and C in the figure. Wave A is the main incident wave propagated from the wave source. Waves B and C are additional waves caused by debonding damage. In this study, four parameters are used to describe the changes in the waveform due to the damage. The arrival time of Wave A is defined as the time interval between the input signal and Wave A. This parameter is used to describe the time delay of Wave A, which is related to the wave speed directly. The amplitude of Wave A is the second parameter to describe the attenuation of wave propagation in the material. The time interval between Waves A and B or Wave A and C is used to describe the time delay of Wave B or C. The amplitude ratio of Wave A to B or Wave A to C is used to describe the amplitude properties of Wave B or C. In the above, the amplitude of the wave is defined as the absolute peak value. The changes of these parameters due to the damage and their sensitivity to damage are studied in the following.

4.1. Effect of the debonding damage

4.1.1. Effect of debonding length

The 5-element model is used in the calculation. The third element is taken as the damaged element and the debonding damage index α_b is equal to 1 that means the full debond of the element. Both the debonding length and location are varied in numerical calculations. There are a total of 55 cases with the debonding length varying from 0.0 to 1.0 m with an increment of 0.1 m; and the debonding location measured from the actuator varying from 0.3 to 1.2 m, also with a 0.1 m increment. The detailed results are summarized in Table 1. Fig. 9 shows the incident waves with different debonding lengths at the debonding location of 0.5 m. The results show that the arrival time of Wave A reduces with the debonding length, and the amplitude increases with the debonding length. These two parameters could be the good indicators of the debonding length. Wave B is moving away from Wave A when the debonding length increases and there is no obvious change in the amplitude of Wave B. The parameters related to Wave C, however, remain unchanged when the debonding length increases. This is because a stress wave will be transferred into two parts: transmitted wave and reflected wave when meeting a discontinuity, or debonding in the present case. The first reflected wave will be produced at the starting location of the debonding damage and it will be reflected again at the wave source, which forms Wave C. Therefore the time interval between Waves A and C is only related to the distance between the wave source and the debonding location. At the end location of the debonding damage, another reflected wave will be formed and it will be reflected again at the starting location, which becomes Wave B. The time interval between Waves A and B is therefore only related to the debonding length.

Fig. 10 shows the relationship between the four parameters and the debonding length when the debonding damage occurs at different locations. Fig. 10(a) shows the arrival times of Wave A for different debonding length at 0.3, 0.5 and 0.8 m. In the figure, the arrive times of Wave A are approximately the same when the debonding is located at 0.3, 0.5 and 0.8 m, respectively. It shows the debonding location, when it is in between the source and receiver, has no effect on the arrival time of Wave A. The arrival time of Wave A reduces with the debonding length and it has approximately a linear relationship. It can be fitted to the following equation:

$$y = px + r \tag{23}$$

The results are $p = -0.252$ and $r = 0.445$. As shown in Fig. 10(a), the fitted line agrees very well to all points. Based on the results, the arrival time of Wave A is only dependent on the debonding length. It could be a good indicator of the debonding length. This is because the interaction between the concrete and steel becomes weaker when the length of the debonding zone increases, resulting in an increase in the wave speed. Fig. 10(b) shows the relationship between the amplitude of Wave A and the debonding length when the debonding is located at 0.4, 0.5 and 0.8 m, respectively. It shows that the debonding location has no effect on the amplitude of Wave A either. However, the wave amplitude depends on the debonding length. The relationship between wave amplitude and debonding length is nonlinear and can be fitted by Eq. (24).

$$y = px^q + r \tag{24}$$

The results are $p = 5.6591$, $q = 1.3225$ and $r = 5.41$. This indicates that the amplitude of Wave A is also a good indicator of debonding length.

Table 1
Results based on the numerical models with different debonding lengths at different locations.

Debonding location (m)	Debonding length (m)	Arrival time (ms)	Amplitude ($\times 10^{-7}$)	Time interval (ms)		Amplitude ratio	
				Waves A and C	Waves A and B	Waves A and C	Waves A and B
No damage	0	0.445	6.010	–	–	–	–
0	0.1	0.42	8.931	0.051	–	3.238	–
	0.2	0.395	9.788	0.089	–	3.457	–
	0.3	0.369	10.42	0.128	–	3.875	–
	0.4	0.343	11.14	0.168	–	4.320	–
	0.5	0.318	12.23	0.206	–	4.900	–
	0.6	0.292	13.44	0.245	–	5.563	–
	0.7	0.267	14.45	0.283	–	6.218	–
	0.8	0.241	15.38	0.321	–	6.937	–
	0.9	0.215	16.62	0.361	–	7.918	–
	1	0.189	19.07	0.397	–	9.142	–
0.1	0.1	0.42	5.679	0.090	–	3.238	–
	0.2	0.394	6.213	0.091	–	4.558	–
	0.3	0.369	6.560	0.090	–	3.454	–
	0.4	0.342	6.926	0.091	–	3.311	–
	0.5	0.317	7.626	0.090	–	3.267	–
	0.6	0.292	8.488	0.090	–	3.375	–
	0.7	0.266	9.149	0.090	–	3.475	–
	0.8	0.24	9.623	0.090	–	3.404	–
	0.9	0.215	10.31	0.089	–	3.278	–
0.2	0.1	0.42	5.677	0.180	–	4.604	–
	0.2	0.394	6.212	0.180	0.077	4.671	8.546
	0.3	0.369	6.561	0.180	0.116	4.509	9.262
	0.4	0.342	6.925	0.180	–	3.998	–
	0.5	0.317	7.624	0.180	–	4.938	–
	0.6	0.292	8.486	0.179	–	4.609	–
	0.7	0.266	9.148	0.180	0.271	4.646	15.97
	0.8	0.24	9.623	0.180	0.310	4.378	17.88
0.3	0.1	0.42	5.677	0.270	–	6.273	–
	0.2	0.394	6.212	0.270	0.077	6.132	8.553
	0.3	0.369	6.560	0.270	0.116	5.785	9.277
	0.4	0.342	6.925	0.271	0.156	5.676	10.08
	0.5	0.317	7.624	0.271	0.194	5.980	11.55
	0.6	0.292	8.486	0.270	–	6.010	–
	0.7	0.266	9.148	0.270	–	4.307	–
0.4	0.1	0.42	5.676	0.360	–	8.190	–
	0.2	0.394	6.212	0.360	0.077	7.928	8.556
	0.3	0.369	6.560	0.360	0.116	7.825	9.284
	0.4	0.342	6.924	0.361	0.156	7.798	10.09
	0.5	0.317	7.624	0.360	0.194	8.036	11.57
	0.6	0.292	8.485	0.360	0.232	7.967	13.60
0.5	0.1	0.42	5.676	0.450	–	10.56	–
	0.2	0.394	6.212	0.450	0.077	10.59	8.559
	0.3	0.369	6.560	0.449	0.116	10.66	9.287

Table 1 (*continued*)

Debonding location (m)	Debonding length (m)	Arrival time (ms)	Amplitude ($\times 10^{-7}$)	Time interval (ms)		Amplitude ratio	
				Waves A and C	Waves A and B	Waves A and C	Waves A and B
	0.4	0.342	6.924	0.451	0.156	10.46	10.09
	0.5	0.317	7.623	0.450	0.194	10.33	11.58
0.6	0.1	0.42	5.676	0.540	–	14.18	–
	0.2	0.394	6.212	0.541	0.077	14.56	8.560
	0.3	0.369	6.560	0.540	0.116	14.30	9.289
	0.4	0.342	6.924	0.541	0.156	13.49	10.10
0.7	0.1	0.42	5.676	0.630	–	19.63	–
	0.2	0.394	6.212	0.631	0.077	19.59	8.561
	0.3	0.369	6.559	0.629	0.116	18.52	9.289
0.8	0.1	0.42	5.676	0.720	–	26.50	–
	0.2	0.394	6.212	0.720	0.077	25.43	8.562
0.9	0.1	0.42	5.676	0.810	–	34.53	–

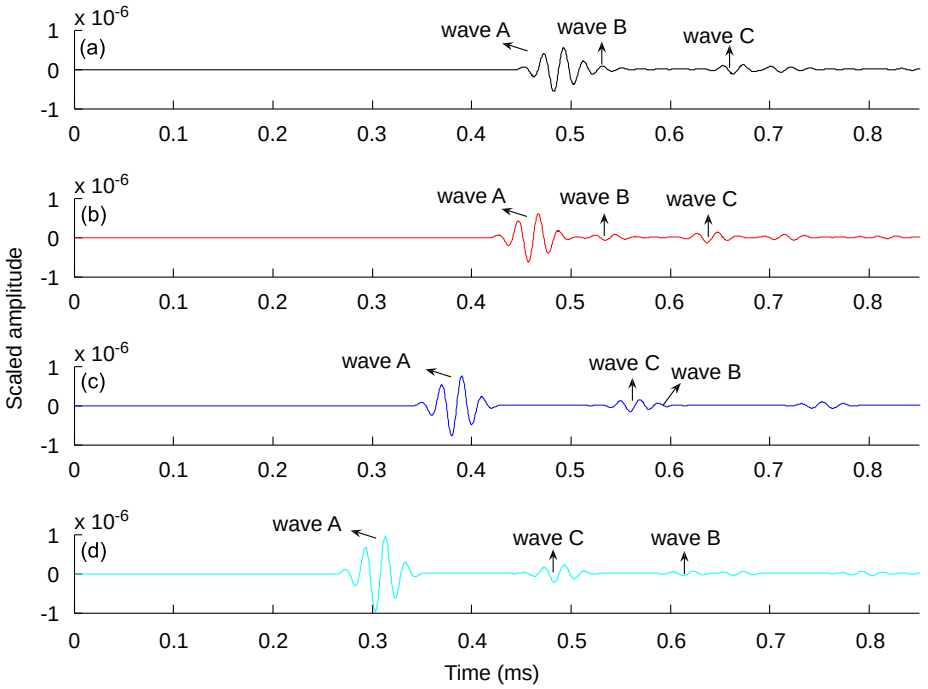

Fig. 9. Received waves with different debonding lengths at the same location (0.5 m): (a) debonding length: 0.1 m; (b) debonding length: 0.2 m; (c) debonding length: 0.5 m; (d) debonding length: 0.8 m.

Fig. 10(c) shows the time interval between Waves A and B when the debonding length changes at different locations, 0.2, 0.3 and 0.5 m, respectively. From the figure, the time intervals are approximately the same when the debonding is at different locations. That shows the debonding location again has no effect on the time

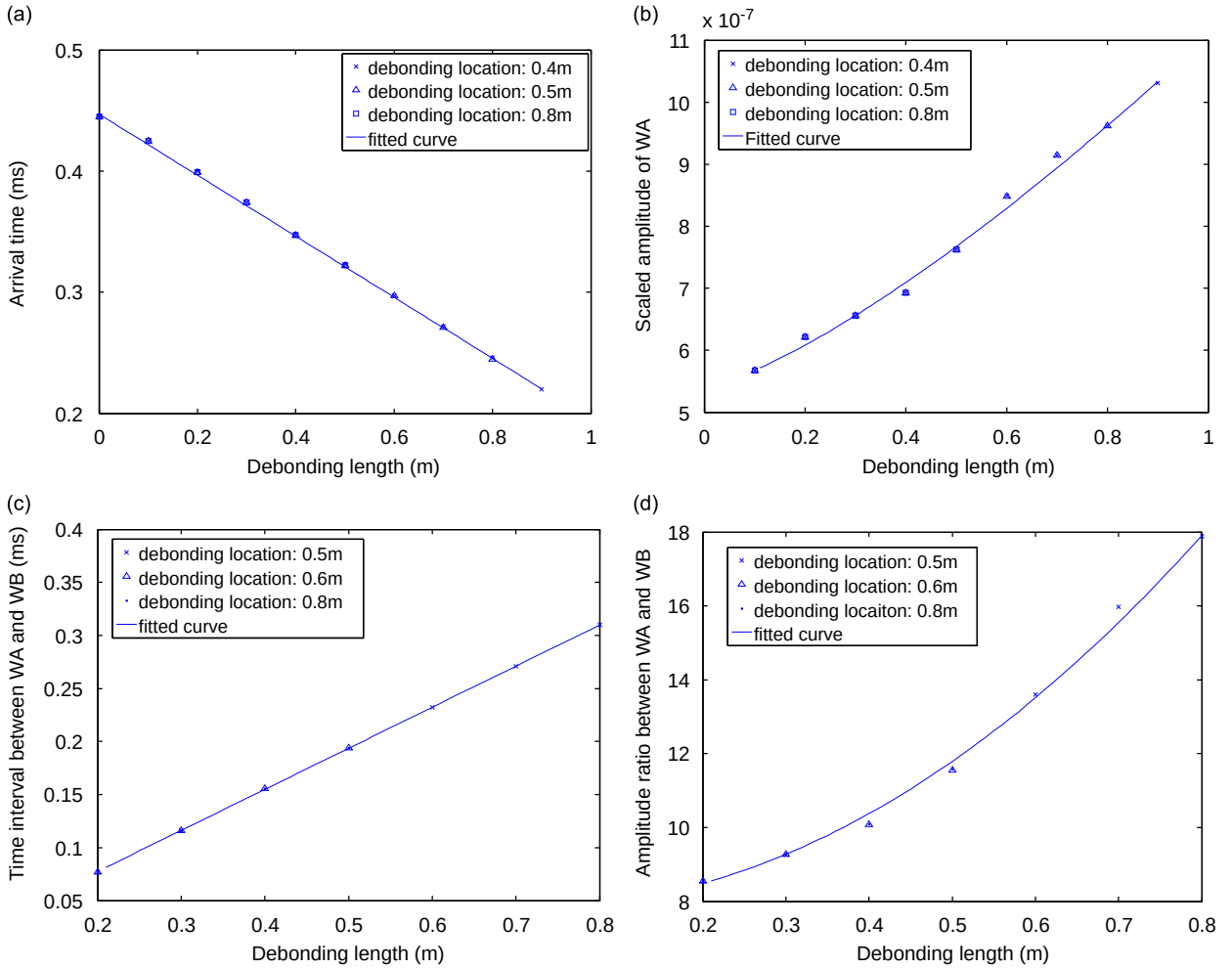

Fig. 10. Relationship between the debonding length and the four parameters: (a) arrival time of Wave A; (b) amplitude of Wave A; (c) time interval between Waves A and B; (d) amplitude ratio between Waves A and B.

interval between Waves A and B. The time interval has approximately a linear relationship with the debonding length as Eq. (23). The parameters are $p = 0.3872$ and $r = 0$. Fig. 10(d) shows the relationship between the amplitude ratio of Waves A and B and the debonding length when the debonding is located at 0.2, 0.3 and 0.5 m from the wave source, respectively. The amplitude ratios are close to each other when the debonding is at different locations, indicating the amplitude ratio is insensitive to the debonding location. But it is influenced by the debonding length. The amplitude ratio is fitted to Eq. (24) with respect to the debonding length. The parameters are $p = 15.69$, $q = 2$, $r = 7.865$.

The results show that the debonding location has no obvious effect on the arrival time, the amplitude of Wave A, and the time interval and the amplitude ratio between Waves A and B. But all these parameters depend on the debonding length, the analytical relationships between debonding length and these parameters are derived based on the numerical simulation results. These relationships can be used as indicators to quantify the debonding length.

4.1.2. Effect of debonding location

From the above analysis, Waves A and B is only related to the debonding length. The corresponding parameters from Waves A and B alone are not sufficient to indicate the debonding location. The new

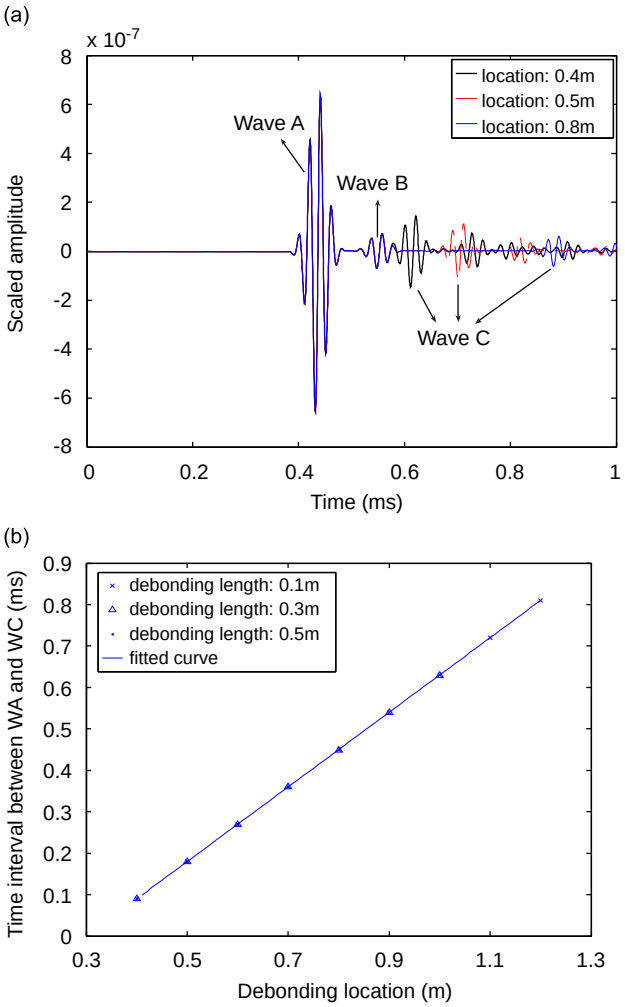

Fig. 11. Effect of the debonding location: (a) received waves with the same debonding length (0.3 m) at different locations; (b) relationship between the debonding location and the time interval between Waves A and C.

parameters are therefore needed to indicate the debonding location. As shown in Fig. 9, there is no obvious change in Wave C for different debonding lengths when the debonding location is the same at 0.5 m from the excitation source. Fig. 11(a) shows the incident waves with the same debonding length at different locations, 0.4, 0.5 and 0.8 m from the excitation source, respectively. In this figure, it shows again that there is no obvious change in Waves A and B. Wave C, however, moves away from Wave A and the amplitude of Wave C reduces with the debonding location moving towards the right direction away from the excitation source. This observation indicates that Wave C depends on the debonding location and its parameters can be used to identify the debonding location.

From the above definition, the time interval between Waves A and C is used to describe the time delay of Wave C, and the amplitude ratio between Waves A and C is used to describe the amplitude change of Wave C. Fig. 11(b) shows the relationship between the time interval and the debonding location when the debonding lengths are 0.1, 0.3 and 0.5 m, respectively. The result shows that the time interval between Waves A and C is the same when the debonding length changes, indicating that the debonding length has no obvious effect on the time interval between Waves A and C. But the time interval has approximately a linear relationship with the debonding location as Eq. (23). The fitted parameters are $p = 0.9$ and $r = 0$. Based on Table 1, although

the amplitude ratio between Waves A and C increases with the debonding location moving to the right away from the excitation source, the parameter fluctuates largely and thus is not suitable for damage detection. This fluctuation is caused by the interaction and coupling of Waves B and C, which becomes more significant and more likely when the debonding occurs at a location towards the right end of the steel bar.

4.1.3. *Effect of the debonding level*

To investigate the effect of α_b on wave propagation, the damage length is taken as 0.5 m and the damage is assumed to occur at the middle of the steel bar, i.e., 0.55 m from the left end. α_b is varied from 0 to 1 for fully bonded and fully debonding scenario, respectively. Fig. 12(a) shows the incident signals with different bonding conditions. As shown, the arrival time of Wave A decreases when α_b reduces. That means the arrival time of Wave A increases when the debonding level decreases. The arrival time of Wave C also decreases when α_b reduces. Fig. 12(b) shows the relationship between the amplitude ratio of Wave A to Wave C and α_b. It is nonlinear and can be fitted to Eq. (24). The results are $p = 5.8$, $q = -1$, and $r = 0$.

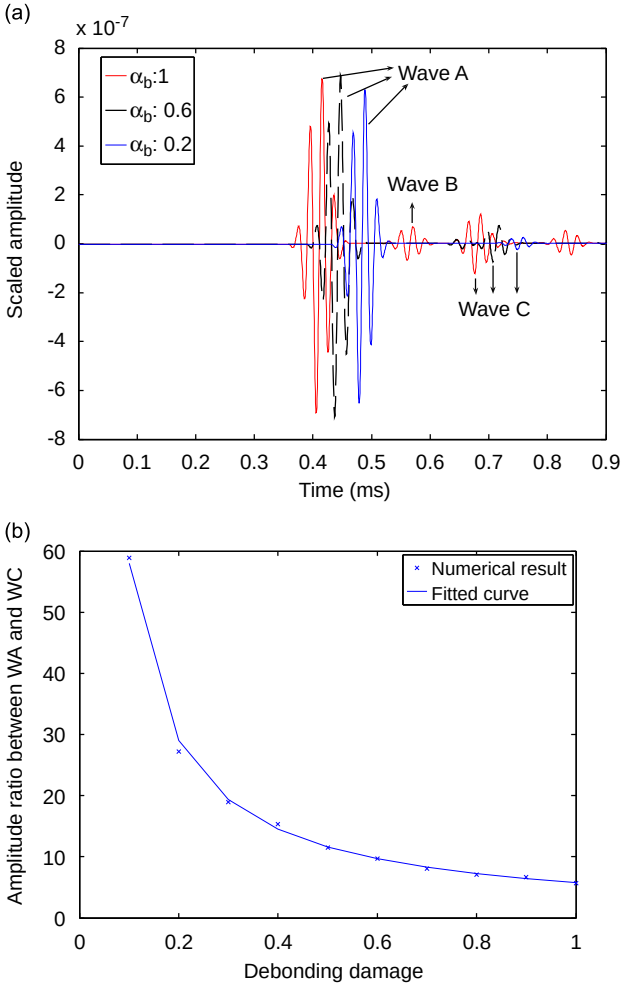

Fig. 12. Effect of the debonding strength: (a) wave propagation along a steel rebar in a concrete beam with different bond damage scenarios; (b) relationship between the amplitude ratio and the debonding damage index.

Table 2
Results based on the model with different α_b.

α_b	Arrival time (ms)	Amplitude ($\times 10^{-7}$)	Time interval (ms)		Amplitude ratio	
			Waves A and C	Waves A and B	Waves A and C	Waves A and B
0	0.445	6.010	–	–	–	–
0.1	0.434	6.504	0.270	–	58.86	–
0.2	0.421	6.518	0.270	–	27.18	–
0.3	0.409	6.696	0.271	–	18.94	–
0.4	0.398	7.193	0.271	–	15.32	–
0.5	0.388	6.966	0.271	–	11.50	–
0.6	0.379	7.093	0.271	0.218	9.663	36.10
0.7	0.371	7.048	0.270	0.201	8.085	24.37
0.8	0.363	7.041	0.270	0.185	7.067	17.37
0.9	0.355	7.159	0.271	0.170	6.690	13.48
1	0.347	6.925	0.271	0.156	5.676	10.08

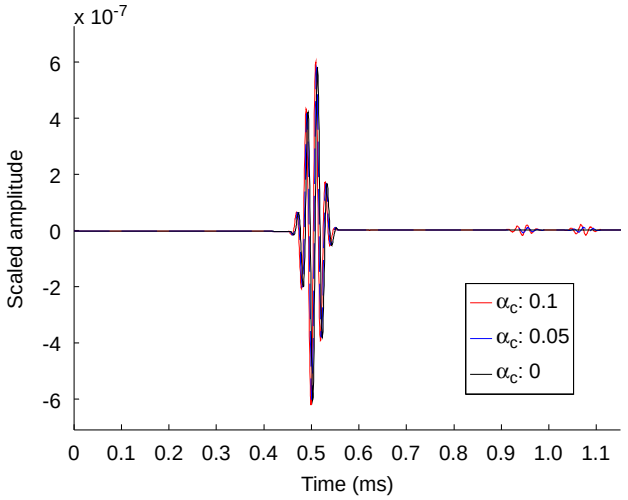

Fig. 13. Wave propagation along a steel rebar in a concrete beam with three different concrete damage scenarios.

Table 2 shows the variation of the six parameters when α_b is varied from 0 to 1. The arrival time of Wave A reduces when α_b increases. However, there is no obvious change in the amplitude of Wave A. The time interval between Waves A and C remains the same when α_b changes. Wave B appears only when α_b is larger than 0.5, and its arrival time decreases when α_b increases. The amplitude ratio between Waves A and C reduces when α_b increases.

4.2. *Effect of the material properties of concrete and steel bar*

Assume α_c changes from 0.0 to 0.1, and the damage is 0.5 m long and is located at 0.55 m from the left end. Fig. 13 shows the wave signals with different concrete damage. In the figure, there is no obvious change in Wave A, and Waves B and C are all very small. In practice, it is more convenient to record the first two waves (A and B) because of their earlier arrival and higher amplitude than Wave C. So only the first two waves are investigated. Table 3 shows the calculated results of four parameters when α_c changes. The arrival time of Wave A reduces when α_c increases. It indicates that when the Young's modulus of concrete decreases, the

Table 3
Results based on the model with different α_c.

α_c	Arrival time (ms)	Amplitude ($\times 10^{-7}$)	Time interval (ms)	Amplitude ratio
0	0.445	6.010	–	–
0.01	0.444	6.169	0.222	574.39
0.02	0.442	6.316	0.223	201.92
0.03	0.44	6.227	0.223	124.96
0.04	0.44	6.014	0.222	89.88
0.05	0.438	6.265	0.223	69.76
0.06	0.436	6.168	0.223	58.35
0.07	0.436	6.128	0.222	49.02
0.08	0.434	6.222	0.223	43.36
0.09	0.433	6.154	0.223	37.96
0.1	0.432	6.107	0.222	34.68

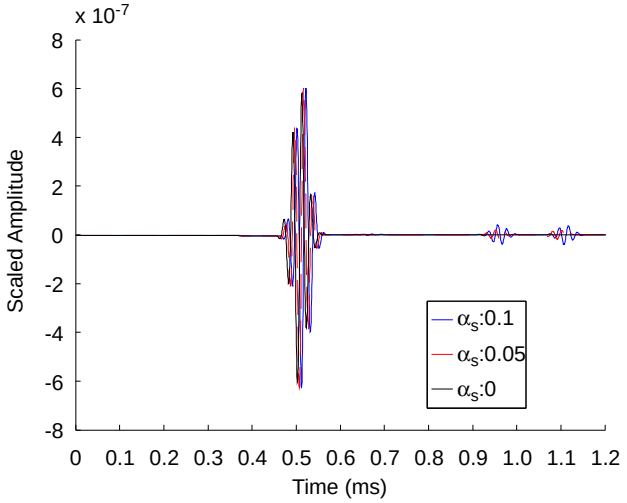

Fig. 14. Wave propagation along a steel rebar in a concrete beam with different steel damage scenarios.

arrival time of Wave A will be reduced, which means the wave speed will increase, which can be explained by Eq. (10). The time interval between Waves A and B remains the same when α_c increases, but the amplitude ratio reduces quickly when α_c increases, indicating that the amplitude ratio is a better indicator of damage in concrete because it is much more sensitive than the arrival time. The amplitude of Wave A fluctuates from 6.01 to 6.32, but it has no direct relation with the concrete damage.

Similar to α_c, α_s is changed from 0.0 to 0.1. The same damage length and location is assumed. Fig. 14 shows the generated incident wave signals with different α_s. The results show that the arrival time of Wave A will increase when the Young's modulus of steel decreases. That means that the wave speed will decrease with α_s. Waves B and C appear nearly simultaneously but their amplitudes become larger when the damage in the steel bar increases. To investigate the effect of steel damage quantitatively, the calculated parameters corresponding to different α_s are shown in Table 4. In the table, time interval value remains a constant for different steel damage. The amplitude of Wave A fluctuates with no apparent rule. The arrival time increases and the amplitude ratio reduces with α_s. These two parameters will be good indicators for steel damage.

Table 4
Results based on the model with different α_s.

α_s	Arrival time (ms)	Amplitude ($\times 10^{-7}$)	Time interval (ms)	Amplitude ratio
0	0.4451	6.010	–	–
0.01	0.448	6.211	0.222	135.85
0.02	0.45	6.254	0.223	75.78
0.03	0.453	6.167	0.223	51.22
0.04	0.456	6.022	0.223	38.88
0.05	0.459	6.023	0.223	31.09
0.06	0.462	6.203	0.222	25.72
0.07	0.465	6.126	0.223	22.17
0.08	0.468	6.301	0.223	19.18
0.09	0.472	6.259	0.222	16.92
0.1	0.476	6.004	0.222	14.95

From the numerical results, α_s and α_c have relatively less effects, as compared to the debonding damage, on wave propagations along a steel bar in a RC structure.

It should be noted that the above parametric analyses are performed based on the assumption that the debonding damage and the material deterioration occurs independently and separately. In practice, debonding and material deterioration, i.e., reduction in elastic modulus, may occur simultaneously. Further studies are needed to differentiate these different damage types. It should also be noted that the above results and observations are made based on the condition that the debonding damage occurs in between the wave source and the receiver. If debonding occurs behind the receiver, it will also affect the recorded signal owing to wave reflection. However, the above observations will not be the same.

5. Conclusions

A concrete–steel spectral element has been developed to analyse wave propagation along a steel rebar in concrete. The wave propagation characteristics corresponding to different structural conditions were analysed. The changes in the wave propagation properties were suggested to be used to identify structural damages. Three damage indices are defined to describe damage in concrete, steel rebar or debonding between the steel rebar and concrete. Laboratory study has been carried out to verify the developed SEM for modeling wave propagations. The results show the model can be used to predict the wave propagation along the steel bar in concrete with complex interaction between the steel rebar and concrete.

The relationships between the damage indices and the wave parameters have also been obtained and they can be used to quantify the damage in RC structures. Several parameters related to Waves A, B and C are proposed and applied to damage detection. Based on the time interval between Waves A and C, the debonding location can be estimated. The amplitude ratio between Waves A and C is a good indicator of the debonding damage index. The amplitude and arrival time of Wave A can be used to determine the debonding length. The relationships between the parameters and damage are obtained and can be used to quantify the damage. It should be noted that the above formulas are based on rod theory. If the steel rebar is thicker, ideal rod theory may be inapplicable due to lateral inertia effect. Further experimental study is needed to obtain the empirical formulas for different geometrical conditions.

Acknowledgment

The work described in this paper was supported from CIEAM through Project ID207.

Appendix A

$$
D = \begin{bmatrix}
0 & 0 & e^{-ik_2L_1} & e^{-ik_2L_2} & 0 & 0 & 0 & 0 & 0 & 0 \\
e^{-ik_1L_1} & 1 & e^{-ik_2L_1} & e^{-ik_2L_2} & 0 & 0 & 0 & 0 & 0 & 0 \\
-ik_1e^{-ik_1L_1} & ik_1 & ik_2e^{-ik_2L_1} & -ik_2e^{-ik_2L_2} & 0 & 0 & 0 & 0 & 0 & 0 \\
0 & 0 & e^{-ik_2(L_1+L_2)} & 1 & -e^{-ik_3(L_1+L_2)} & -e^{-ik_3L_3} & 0 & 0 & 0 & 0 \\
0 & 0 & -ik_2e^{-ik_2(L_1+L_2)} & ik_2 & ik_3e^{-ik_3(L_1+L_2)} & -ik_3e^{-ik_3L_3} & 0 & 0 & 0 & 0 \\
0 & 0 & 0 & 0 & e^{-ik_3(L_1+L_2+L_3)} & 1 & -e^{-ik_4(L_1+L_2+L_3)} & -e^{-ik_4L_4} & 0 & 0 \\
0 & 0 & 0 & 0 & -ik_3e^{-ik_3(L_1+L_2+L_3)} & ik_3 & ik_4e^{-ik_4(L_1+L_2+L_3)} & -ik_4e^{-ik_4L_4} & 0 & 0 \\
0 & 0 & 0 & 0 & 0 & 0 & -ik_4e^{-ik_4(L_1+L_2+L_3+L_4)} & ik_4 & ik_5e^{-ik_4(L_1+L_2+L_3+L_4)} & -ik_5e^{-ik_5L_5} \\
0 & 0 & 0 & 0 & 0 & 0 & e^{-ik_4(L_1+L_2+L_3+L_4)} & 1 & e^{-ik_5(L_1+L_2+L_3+L_4)} & e^{-ik_5L_5} \\
0 & 0 & 0 & 0 & 0 & 0 & e^{-ik_4(L_1+L_2+L_3+L_4)} & 1 & 0 & 0
\end{bmatrix}
$$

References

[1] J.N. Barshinger, J.L. Rose, Guided wave propagation in an elastic hollow cylinder coated with a viscoelastic material, *IEEE Transactions on Ultrasonics, Ferroelectrics and Frequency Control* 51 (11) (2004) 1547–1556.

[2] J.F. Doyle, *Wave Propagation in Structures: Spectral Analysis Using Fast Discrete Fourier Transforms*, Springer-Verlag, New York, 1997.

[3] K.F. Graff, *Wave Motion in Elastic Solids*, Clarendon Press, Oxford, 1975.

[4] V. Giurgiutiu, A. Cuc, Embedded non-destructive evaluation for structural health monitoring, damage detection, and failure prevention, *The Shock and Vibration Digest* 37 (2) (2005) 83–105.

[5] S.D. Kim, C.W. In, K.E. Cronin, H. Sohn, K. Harries, Reference-free NDT technique for debonding detection in CFRP-strengthened RC structures, *Journal of Structural Engineering, ASCE* 133 (8) (2007) 1080–1091.

[6] M. Krawczuk, J. Grabowska, M. Palacz, Longitudinal wave propagation. Part I—comparison of rod theories, *Journal of Sound and Vibration* 295 (3–5) (2006) 461–478.

[7] S.J. Lee, H. Sohn, Active self-sensing scheme development for structural health monitoring, *Smart Materials and Structures* 15 (2006) 1734–1746.

[8] M.J.S. Lowe, Matrix techniques for modelling ultrasonic waves in multilayered media, *IEEE Transactions on Ultrasonics, Ferroelectrics and Frequency Control* 42 (4) (1995) 525–541.

[9] M. Mitra, S. Gopalarishnan, Wavelet based spectral finite element modelling and detection of de-lamination in composite beams, *Proceedings of the Royal Society of London, Series A: Mathematical, Physical and Engineering Sciences* 462 (2006) 1721–1740.

[10] F. Moser, L.J. Jacobs, J. Qu, Modeling elastic wave propagation in waveguides with the finite element method, *NDT&E International* 32 (4) (1999) 225–234.

[11] J.M. Muggleton, T.P. Waters, B.R. Mace, B. Zhang, Approaches to estimating the reflection and transmission coefficients of discontinuities in waveguides from measured data, *Journal of Sound and Vibration* 307 (1–2) (2007) 280–294.

[12] W.B. Na, T. Kundu, M.R. Ehsani, Lamb Waves for detecting delamination between steel bars and concrete, *Computer-Aided Civil and Infrastructure Engineering* 18 (1) (2003) 58–63.

[13] W.M. Ostachowicz, Damage detection of structures using spectral finite element method, *Computers and Structures*, (2007). doi:10.1016/j.compstruc.2007.02.004.

[14] M. Palacz, M. Krawczuk, Analysis of longitudinal wave propagation in a cracked rod by the spectral element method, *Computers and Structures* 80 (2002) 1809–1816.

[15] M. Palacz, M. Krawczuk, W. Ostachowicz, Detection of additional mass in rods: experimental and numerical investigation, *Archive of Applied Mechanics* 74 (2005) 820–826.

[16] A. Raghavan, C.E.S. Cesnik, Review of guided-wave structural health monitoring, *The Shock and Vibration Digest* 39 (2) (2007) 91–114.

[17] C.K. Soh, S.P. Chiew, Y.X. Dong, Damage model for concrete–steel interface, *Journal of Engineering Mechanics, ASCE* 125 (8) (1999) 879–883.

[18] C.K. Soh, Y. Liu, Y.X. Dong, X.Z. Lu, Damage model based reinforced concrete element, *Journal of Materials in Civil Engineering, ASCE* 15 (4) (2003) 371–380.

[19] F. Wu, F.K. Chang, Debond detection using embedded piezoelectric elements in reinforced concrete structures—part 1: experiment, *Structural Health Monitoring* 5 (1) (2006) 5–15.

[20] F. Wu, F.K. Chang, Debond detection using embedded piezoelectric elements in reinforced concrete structures—part II: analysis and algorithm, *Structural Health Monitoring* 5 (1) (2006) 17–28.

[21] X.Q. Zhu, S.S. Law, A concrete–steel interface element for damage detection of reinforced concrete structures, *Engineering Structures* 29 (12) (2007) 3515–3524.